Dynamics of a turbulent spin-down flow inside a torus

Vitaly Noskov,[1] Rodion Stepanov,[1] Sergey Denisov,[1] Peter Frick,[1] Gautier Verhille,[2] Nicolas Plihon,[2] and Jean-François Pinton[2]
[1]*Institute of Continuous Media Mechanics, Korolev 1, Perm 614013, Russia*
[2]*Laboratoire de Physique de l'École Normale Supérieure de Lyon, CNRS and Université de Lyon, F-69364 Lyon, France*

(Received 25 November 2008; accepted 24 March 2009; published online 27 April 2009)

A turbulent screw flow (with Reynolds number exceeding 10^6) is generated by the sudden stop of a toroidal channel. The working fluid is a gallium alloy and velocity measurements are performed using a dual-axis potential probe. We describe the onset of motion, the development of strongly anisotropic fluctuations, and the final homogenization and decay of turbulence. Our observations are relevant for the relaxation of anisotropic turbulence; they are also in agreement with measurements of magnetohydrodynamic induction processes in this type of flow. © *2009 American Institute of Physics*. [DOI: 10.1063/1.3123529]

I. INTRODUCTION

Many turbulent flows considered as *stationary homogeneous and isotropic* are forced in reality by isolated intrinsically *nonstationary* events, and each of them can be characterized by strong anisotropy. *Globally* the statistical properties can strictly satisfy the requirements of isotropy, but local motions can be dramatically different. Efficient schemes using local or time dependent anisotropy have been proposed for mixing[1] or dynamo purposes.[2] We examine the evolution of statistical properties of small-scale fluctuations in a nonstationary flow generated in a toroidal channel. The spin-down regime of the flow generated inside a torus has recently received some attention in the context of dynamo research.[3–5] In the experimental setup, a hollow, liquid-filled torus is rotated about its main axis and suddenly brought to a halt by strong braking. A screw flow results, and it can be enhanced by the presence of helical diverters inside the torus. This screw flow is potentially capable of generating a dynamo.[6] In this magnetohydrodynamics (MHD) instability problem, a global conversion from kinetic energy into magnetic energy is expected to occur when the stretching of magnetic field lines overcomes dissipation. The properties of the velocity field are thus essential. Numerical simulations are exhaustive but limited to the neighborhood of the laminar regime.[6,7] As dynamo action develops for sufficiently intense motions which make the flow fully turbulent, one needs to characterize the fluid's motions at all scales for which the induction processes are expected to be efficient. In this study, we analyze velocity measurements made with a gallium alloy as working fluid. The goal is to characterize the flow dynamics in the same situation as used for the study of MHD processes by taking advantage of a velocimetry technique than can operate in opaque, electrically conducting, and highly thermally conducting media. Velocity measurements in liquid metals are essential for a better understanding of the elementary induction and dynamo processes in turbulent flows. We shall discuss the onset of the flow, the isotropy of the motions, and the development and decay of its small-scale turbulence. This work will be divided into two main parts: the first one is a presentation of the experimental setup and of the measurement method, while the second part discusses the dynamics of the flow.

II. SETUP AND MEASUREMENT TECHNIQUE

A. Perm torus flow

A schematic diagram of the setup is given in Fig. 1. It consists of a toroidal channel filled with liquid metal (a gallium alloy) (1) made of an electrically insulating material (textolite). The channel is fastened to a horizontal axle, rotated by an electric motor (5). A disk braking system (6) is fixed on the same axle. Initially, the fluid together with the toroidal channel is set in solid body rotation at a constant rotation rate which can be as high as 55 rps (revolutions per second). The mechanical braking system stops the vessel in about 0.1 s and thrusts the fluid into motion with respect to the vessel. The fluid velocity is initially mainly along the toroidal direction (along the channel); then a poloidal component develops (even when no diverter is inserted inside the channel as in the case of the present study) before motions ultimately decay under viscous dissipation.

The large radius of the torus is $R=0.0875$ m, with a small radius $r_0=0.0225$ m; the net mass of liquid metal is 5.58 kg. In practice, we have used a Ga–Zn–Sn alloy, made of 2% of Zn and 10.5% of Sn, with the advantage of a melting point at 19 °C. The rotation rate F of the channel is adjusted between 30 and 55 rps (we shall also use the angular velocity $\Omega=2\pi F$). The accuracy of the rotation rate control is equal to 0.5 rps. Both clockwise and anticlockwise rotations can be achieved. The torus is halted in a short braking time which varies with the initial rotation frequency from 0.057 up to 0.107 s when the rotation rate grows from 35 to 55 rps. For each given rotation rate the braking time is constant up to ± 0.005 s. The torus angular speed is recorded using an optical tachometer; it monitors the disks on which the brakes act. The Reynolds number of the flow, based on the channel size and initial toroidal speed, $\mathrm{Re}=\Omega R r_0/\nu$ with $\nu=7\times10^{-7}$ the viscosity, is of the order of 10^6, so one expects a fully turbulent flow to develop.

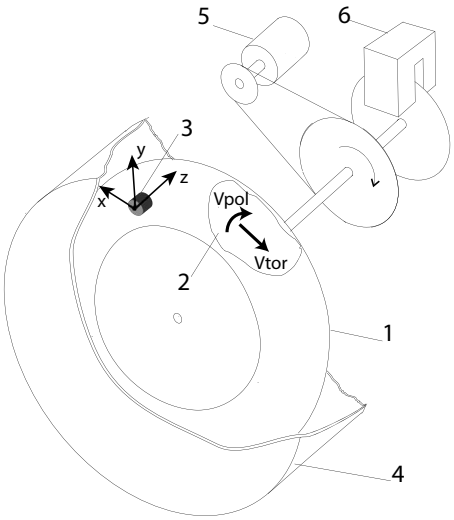

FIG. 1. Experimental setup: (1) flow vessel, made of insulating textolite; (2) toroidal channel; (3) velocity probe mounted on the channel wall; (4) security shield; (5) driving motor; (6) mechanical brakes. Note that helical diverters are *not* inserted inside the channel

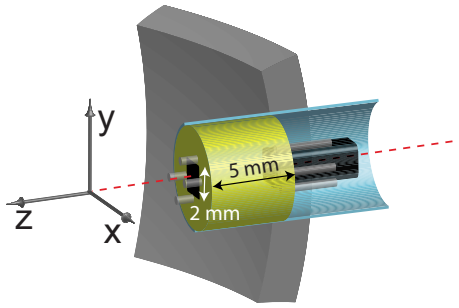

FIG. 2. (Color online) Schematics of the potential probe. The permanent NdFeB magnet (in black, size $2\times2\times10$ mm^3) imposes a 0.2 T magnetic field at the surface).The four electrodes are made of tungsten wires (diameter 500 μm, length 2 mm) and allow a two-axis measurement of the velocity in the plane perpendicular to the axis of the magnet (v_x,v_y).

B. Velocity measurements

Previous studies of this flow relied on measurements using a water prototype and particle tracking velocimetry techniques[5] with large-scale tracer particles (size of about 1 mm). This gives an accurate picture of the decay of the mean toroidal velocity field in the spin-down flow in the channel with or without helicity generating diverters, but the technique was limited in regards to accessible time dynamics and resolution of small-scale motions. Here we use a two-axis local probe designed to provide a good dynamical resolution of toroidal and poloidal motions and operating in liquid metals.

We perform velocity measurements using potential probes. The method relies on linking the potential difference measured between two electrodes to local characteristics of the velocity field or its gradients. Previous investigations have shown that this is indeed possible when electrodes are set in the vicinity of a localized strong permanent magnet B_0.[8–11] Two situations can then be distinguished:

- If the electrodes are arranged so as to estimate the Laplacian $\Delta\phi$ of the potential field, then the divergence of Ohm's law yields $\Delta\Phi=\vec{\nabla}\cdot(\vec{u}\times\vec{B})$, where $\vec{u}$ is the velocity field. Under conditions such that the induced magnetic field is much smaller than the imposed field B_0, then $\Delta\Phi=\vec{\omega}\cdot\vec{B}_0$, with $\vec{\omega}=\vec{\nabla}\times\vec{u}$, and the measurement probes the component of the vorticity in the direction of the applied field.[9]
- If one records the potential difference between two points, one probes $\Phi_{AB}=\int_A^B\vec{\nabla}\varphi\vec{dl}$ with $\vec{\nabla}\varphi=\vec{u}\times\vec{B}-\vec{j}/\sigma-\partial\vec{A}/\partial t$, with $\vec{j}$ the current density, σ the electrical conductivity of the liquid, and $\vec{A}$ the vector potential. Under the condition of a strong imposed field localized around the electrodes[10] and the assumption of slow enough motions and vanishingly small current density otherwise induced, the potential difference yields $\Phi_{AB}=\int_A^B(\vec{u}\times\vec{B})\cdot\vec{dl}$.

A schematic of the probe is shown in Fig. 2. The potential difference between two pairs of electrodes provides a measurement of $\int(\vec{u}\times\vec{B})\cdot\vec{dl}$ along two perpendicular axes, x and y. Independent measurement of magnetic induction (using Hall probes) in a similar channel has shown that the *effective* magnetic Reynolds number ($B^{\text{induced}}/B^{\text{applied}}$) is of the order of 10^{-2}, which justifies the vanishingly small current density approximation. The approximation of "slow enough motions" yields a cut-off frequency for the velocity measurement, also set by the separation of the electrodes and the size of the magnet. The potential difference between two electrodes is proportional to the local velocity when $|\partial\vec{A}/\partial t|\ll|\vec{u}\times\vec{B}|$. The cut-off frequency is thus $f_c\sim vB^{\text{applied}}/A$ ($A\sim B^{\text{induced}}\ell_B$, where ℓ_B is a typical length of variation of the magnetic field). Using $\Delta\vec{A}+\mu_0\vec{j}=0$ and our small magnetic Reynolds number approximation of low current density yields $f_c\gg1/\mu_0\sigma\ell_B^2$. Taking $\ell_B=d$, where $d\sim1$ mm is the width of the magnet, we get $f_c\sim20$ kHz, high enough to resolve most of the turbulent motions. Altogether, by measuring the difference of potential between two electrodes one obtains an average of the velocity between them; for instance,

$$\varphi_{x1}-\varphi_{x2}=\int v_yB_zdx, \tag{1}$$

making it clear again that the spatial resolution of the measurement is given by the electrode spacing and, hence, the size of the magnet. In this measurement, the velocity is also averaged over the length of the electrode (as in conventional hot-wire anemometry). Note here that we have favored the use of a local magnet embedded in the probe rather than an externally imposed large-scale field as in other studies[12] for which the relationship between potential measurement and local velocity gradients is uncertain.[9] Thermoelectrically induced voltages have been checked to be negligible under conditions of the present study (see Ref. 10 for a detailed review of experimental challenges of potential measurements in liquid metals).

The probe is mounted on the channel wall and sticks out 5 mm inside the channel so that the measurements are done away from the boundary layers for any phase of the nonstationary flow evolution. The primary (direct) output voltage $\delta\varphi \sim vB_0 d$ is low, of the order of 200 μV sec/m. It is immediately fed into a differential amplifier AD8221 with a gain of 100, located inside the probe. The signal is then digitized with a 12 bit Advantech PCL-1800 digitizer with a 66 666 Hz sampling frequency. The dynamical range of the measurement exceeds 65 dB.

Making use of the Taylor hypothesis (when applicable, i.e., when there is a mean flow) this probe can access large and small-scale velocity fluctuations. Estimates, based on traditional turbulence relationships, lead to Reynolds numbers of the order of $\mathrm{Re} \sim 10^6$, with integral turbulent scale $L \approx 0.04$ m and Kolmogorov scale $\eta \sim 10^{-5}$ m. Using an advection velocity $U \sim 10$ m/s this corresponds to a range of frequencies $200 < f < 10^6$ Hz. However, the smallest scale resolved by the probe is fixed by the electrode spacing (about 1 mm) corresponding to an upper frequency limit $f_{\mathrm{up}} \sim 20$ kHz.

The probe is mounted inside the channel, the probing region being 5 mm away of the channel wall ($z=5$ mm). The probe orientation is such that, ideally, its x axis (Fig. 2) is parallel to the local toroidal direction (along the channel) and its y axis is in the poloidal direction (perpendicular to it, as shown in Fig. 1). In reality there is a small angle θ between the (x,y) and (toroidal,poloidal) coordinates. This angle θ is determined experimentally by spinning the torus in alternate directions of rotation and computing the symmetric and antisymmetric components of the velocities; one then requires that the antisymmetric part be as small as possible. We find $\theta = 6°$, with a precision of about 0.5°. In this procedure, a calibration factor is also tuned to match the toroidal velocities measured in a water prototype.[5] In the sequel we use the corrected velocity values which we call v^{tor} and v^{pol}.

III. RESULTS

A. Flow characteristics

Raw measurements of the toroidal and poloidal velocities, together with the tachometer signal, are reported in Fig. 3 for one typical run. One recognizes a first stage of braking during which the fluid toroidal velocity increases with respect to the halting vessel—as the probe is attached to the vessel, the measurement is performed in this initially moving frame of reference and the initial zero value of the fluid velocity corresponds to solid body rotation. The largest toroidal fluid velocity is reached as the vessel stops; subsequent dynamics are then measured in a frame at rest. In this process, a transverse (poloidal) velocity has developed. Fluid motions subsequently decay under wall and bulk viscous frictions. Questions that can be addressed with such velocity recordings concern the generation of the poloidal flow, the isotropy of the small-scale motions, and the possibility of a late "universal" stage of decay.

We have performed such runs for initial rotation rates of the torus between 30 and 55 rps in clockwise or anticlockwise direction. The corresponding variations of the toroidal and poloidal velocities, averaged over 20 runs for each initial rotation rate, are shown in Fig. 4. Several general features can be observed.

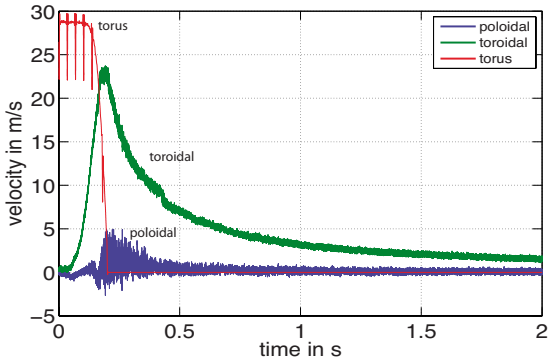

FIG. 3. (Color online) Typical velocity measurement. Blue: poloidal velocity component. Green: toroidal component. Red: torus (peaks mark each full turn of the vessel). Temporal evolutions are shown for a single realization. Initial rotation rate of the torus: 55 rps.

For the toroidal velocity the following are observed.

- The maximum value is set by the initial rotation rate; to leading order we have $v^{\mathrm{tor}}_{\mathrm{max}} \sim R\Omega$, in agreement with

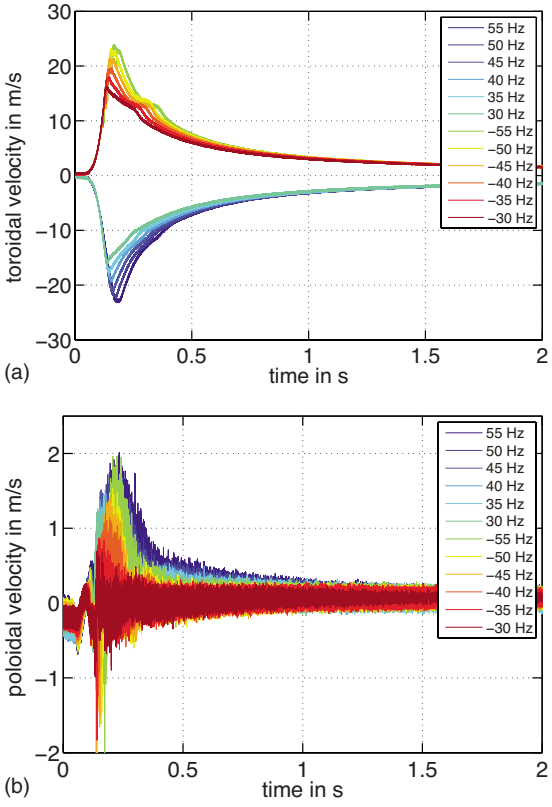

FIG. 4. (Color online) Velocity signal, toroidal and poloidal. Toroidal component: positive curves correspond to a rotation in anticlockwise (−) direction whereas negative data are clockwise (+) rotation. The sign of the poloidal component is independent of the direction of rotation of the torus. For all curves, in absolute value the faster the rotation is the higher the maximum of the curve is. For each initial speed 20 runs have been averaged. The Reynolds number is quite large for both components: it is $\mathrm{Re} \sim 10^6$ based on the maximum toroidal speed and $\mathrm{Re} \sim 10^5$ using the maximum poloidal speed. Here and in the next two figures, $t=0$ is defined as the onset of motion.

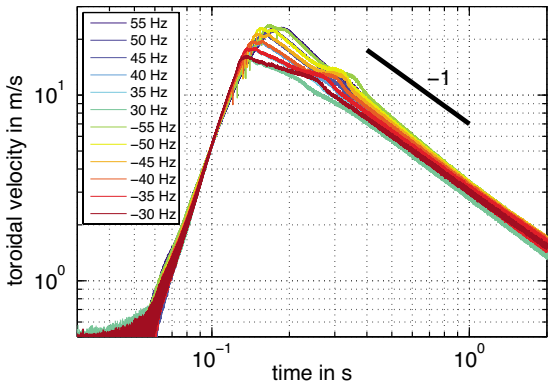

FIG. 5. (Color online) Decay of toroidal velocity. Clockwise torus rotation rates: 30, 35, 40, 45, 50, and 5 rps. The solid line shows a t^{-1} scaling behavior.

previous measurements in a prototype water channel.[5]

- When runs are averaged (as shown in Fig. 4) the toroidal velocity rapidly converges to a mean behavior. We attribute this rather deterministic evolution of the toroidal velocity to the successive action of inertia which initiates the motion with respect to the vessel and the later viscous friction of the fluid on the torus surface which slows it down. A log-log plot of the time variation of the toroidal velocity actually shows a behavior consistent with a $v^{\mathrm{tor}}(t) \sim t^{-1}$ temporal evolution—see Fig. 5. This behavior can be expected from the action of a (quadratic) friction force. It is also the behavior for the free decay of homogeneous turbulence with fixed integral scale—indeed, the Kolmogorov picture of energy transfers leads to $dE/dt \propto E^{3/2}$ for the evolution of the turbulent kinetic energy.

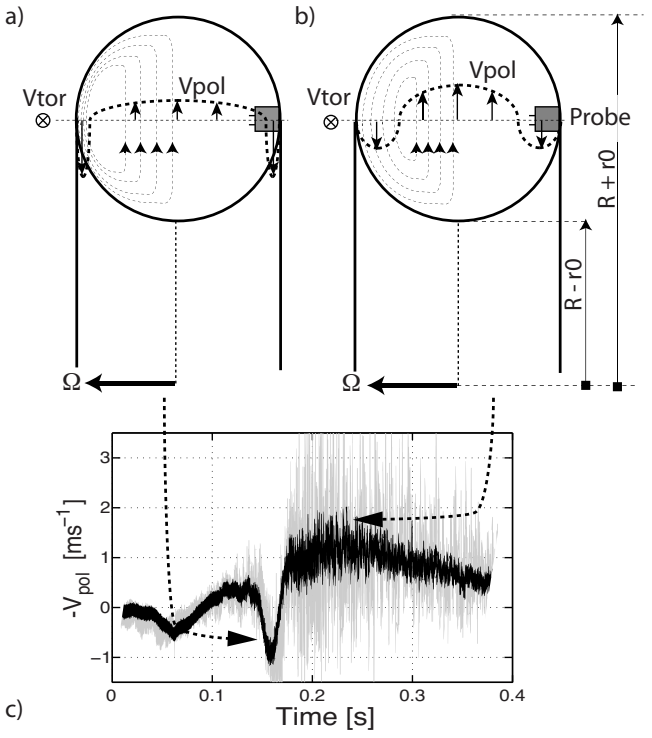

FIG. 6. Schematics of the poloidal flow as it (a) grows initially under the action of the Coriolis force and then (b) from the curved channel instability. (c) Temporal evolution for a single realization (light gray curve) and averaged over 20 realizations (black curve) for an initial driving at 55 Hz.

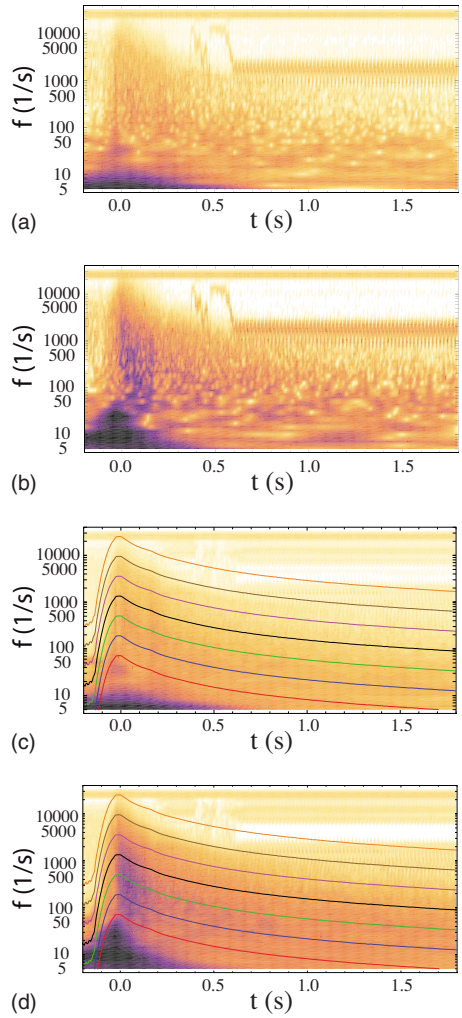

FIG. 7. (Color online) Wavelet spectrogram of velocity dynamics: (a) one realization, toroidal velocity; (b) one realization, poloidal velocity; (c) toroidal averaged over 20 realizations; (d) poloidal average of 20 realizations. The solid lines represent scales of motions that correspond to a given length scale ℓ, computed using the mean toroidal velocity as $f_\ell(t) = \langle v^{\mathrm{tor}} \rangle(t)/\ell$—here $\ell/2r_0 = 0.1$, 1, 2, 5, 10, and 50 (top to bottom).

For the poloidal velocity, the following features are observed.

- The behavior of the poloidal velocity component is more complex. The braking phase corresponds to the injection of energy into poloidal fluid motions. One first observes in Fig. 4 that the poloidal motion always starts in the same (negative) direction, even when the rotation of the vessel is initially reversed. This is understood if one attributes it to the action of a Coriolis force as the vessel decelerates (i.e., nonzero global rotation $\vec{\Omega}$) while at the same time the fluid starts moving with respect to the vessel (nonzero toroidal velocity $\vec{v}^{\mathrm{tor}}$). As both change sign when the rotation of the torus is reversed, $\vec{\Omega} \times \vec{v}^{\mathrm{tor}}$ is unchanged. In addition,

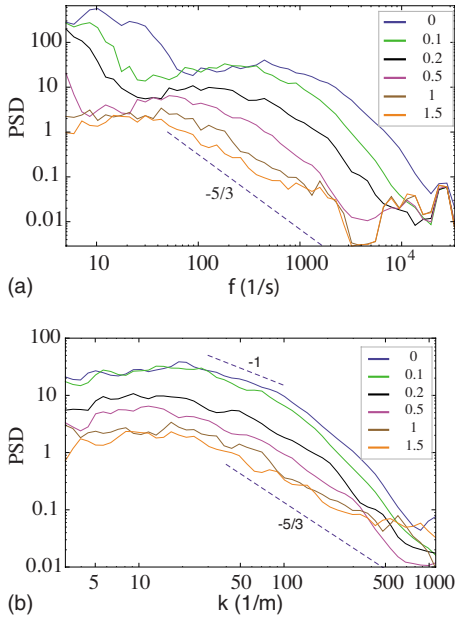

FIG. 8. (Color online) Power spectral density of velocity fluctuations: (a) time spectra, obtained as vertical cross section of the wavelet transforms shown in Fig. 7 for times (in seconds) indicated in the legend; (b) corresponding spectra for spatial distribution of energy, from a local Taylor hypothesis using the toroidal velocity. The dashed line corresponds to -1 and $-5/3$ scalings expected in boundary layers and for homogeneous, isotropic turbulence.

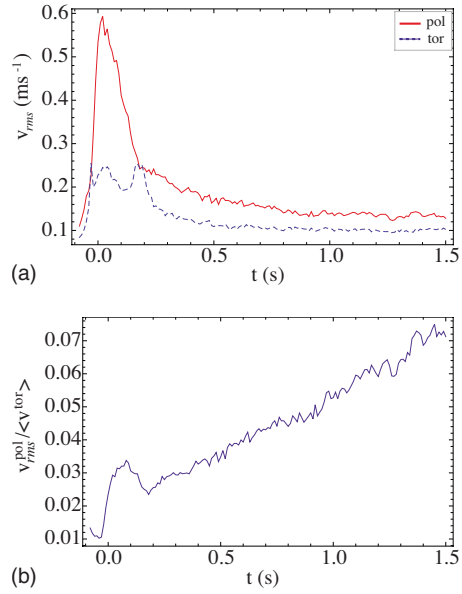

FIG. 9. (Color online) Temporal evolution of (a) poloidal and toroidal rms, defined in the band $20<k<1000$ m^{-1} ($\ell>2r_0$); (b) turbulence level defined as $v_{\mathrm{rms}}^{\mathrm{pol}}/\langle v^{\mathrm{tor}}\rangle$.

we find that the largest negative value of v^{pol} is reached when Ωv^{tor} is also maximum.

- The next phase of motion is also quite deterministic and corresponds to the instability of a flow in a curved channel.[13] The flow is driven radially outward in the center of the channel and recirculates along the walls. The poloidal circulation is shown in Fig. 6 as it evolves from the initial action of Coriolis forces. Initially most of the fluid is moving outward, while at later stages a thicker boundary layer forms. The potential probe is at first above the boundary layer and measures a negative poloidal velocity but it subsequently lies within the recirculation loop and then measures a positive poloidal velocity (as expected from Ref. 13).
- After these two deterministic phases at onset of motion, energy is transferred through the nonlinear terms of the Navier–Stokes equation in a disordered sequence. As we shall see, all scales of motions are excited in the initial phase, so that all participate to the energy transfers.

Finally, we have observed a small but noticeable asymmetry between runs performed with initial clockwise and anticlockwise directions of the rotation of the torus. It was not expected beforehand and may be due to mechanical differences. In the sequel we will focus on data collected with an initial clockwise rotation of the torus.

B. Turbulent dynamics

As noted above, the early stage of flow motion can be understood from simple fluid mechanics principles and we will see that the final stage corresponds to the decay of isotropic turbulence in a channel flow. In this section we focus on the intermediate stage in which a strongly anisotropic turbulence is generated and then decays.

Time-scale representations are convenient to show how fluctuations develop across scales. In Fig. 7 we show a wavelet transform of the time evolution of the toroidal and poloidal velocity components for a single run and averaged over 20 realizations. One observes a very rapid growth of fluctuations at all scales as the channel is halted. The end of breaking ($t=0$ in the figure) also corresponds to the widest spectral content, followed by a long decay phase. Wavelet spectrograms for each realization also reveal unwanted high frequency noise which we filter out in the following analysis.

We first discuss the distribution of kinetic energy among scales (in space and time) using measurements at $F=55$ rps as an example. We use the poloidal component of the velocity since it is absent before the torus is stopped and it develops from nonlinear transfers. The evolution of the spectra in time, Fig. 8(a), show that (i) the energy content is broadest at the time when the channel has stopped and (ii) motions then slow down with the development of a scaling region at later times. The picture is clearer in the spatial spectral space, built using a Taylor hypothesis at the local toroidal velocity, shown in Fig. 8(b). In the initial stage, during breaking, the k spectrum is filled with an almost flat distribution, down to small scales (above about 3 mm). At the end of breaking, ($t\sim 0.1$ s) one observes a range of scale with a "-1" spectral slope at the intermediate range of scales, as is often the case in turbulent boundary layers, the largest energy content is reached with a maximum at $k=22$ m^{-1}, corresponding to a length scale of $2r_0$, equal to the channel diameter. For times larger than about 0.5 s, the spa-

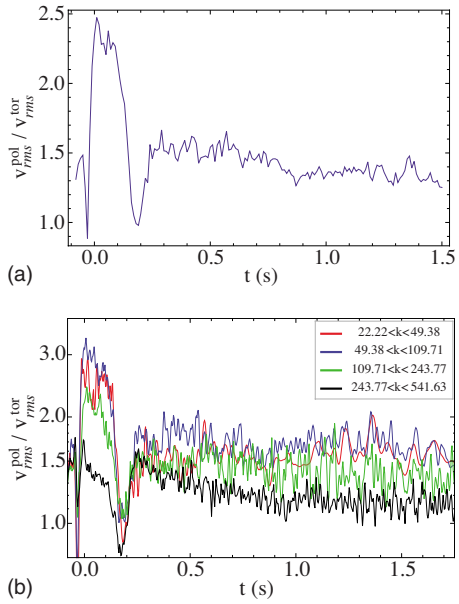

FIG. 10. (Color online) Temporal evolution of (a) anisotropy of velocity fluctuations defined as $v_{\mathrm{rms}}^{\mathrm{pol}}/v_{\mathrm{rms}}^{\mathrm{tor}}$ (for $20<k<1000$ m^{-1}); (b) the same for selected frequency bands.

tial spectra show a range of scale consistent with a "−5/3" scaling characteristic of the decay of three-dimensional (3D) turbulence.

Further informations about the development of turbulence can be drawn from the evolution of toroidal and poloidal velocity fluctuations. To take into account the nonstationarity of the flow, we have defined the fluctuation level of the rms amplitude of after band-pass filtering of the signals. The two corner frequencies of this band-pass filter in k space are $2r_0$ and $r_0/25$, i.e., $20<k<1000$ m^{-1}—a band of frequencies between two corresponding lines in the wavelet transform in Fig. 7—$r_0/25$ also corresponds to the spatial filtering scale due to the probe size. Note a faster decay of toroidal fluctuations compared to poloidal. One also observes (during the time span of the measurement) a slow growth of the ratio $v_{\mathrm{rms}}^{\mathrm{pol}}/\langle v^{\mathrm{tor}}\rangle$, as is shown in Fig. 9.

The isotropy of the flow is also an interesting issue. From our two-axis measurement, we define it as the ratio of the standard deviations of the poloidal and toroidal components. Figure 10(a) shows that the anisotropy of the flow is large at the onset of motions (during and slightly after the stopping phase). It first drops sharply and then decays only slowly. In fact, all scales do not relax toward isotropy at the same rate. This is evidenced by band passing the velocity signals in bands corresponding to different k-space intervals. As shown in Fig. 10(b), the small scales have reach isotropy at $t\sim 1$ s while the large scale relaxes on much longer time scales (outside of the measurement window).

Finally, we comment on the statistics of the poloidal velocity component. Figure 11 shows the evolution of their probability density functions (pdfs), computed during the four major phases the flow dynamics: (I) the braking phase characteristic of energy injection ($t<0$), (II) the development of strongly anisotropic velocity fluctuations ($0<t<0.25$ s), (III) the homogenization toward an isotropic 3D turbulence ($0.35<t<1$ s), and (IV) the late stage of decay ($t>1$ s). Times above are given using measurements at the fastest rotation rate $f=55$ rps as an example. During the braking phase, while the poloidal motion is weak (the distribution is peaked at zero) two processes seem to be at work. The secondary peak at $v^{\mathrm{pol}}\sim -1$ m/s is due to the initial onset of motion. High positive velocities, with an exponential distribution, are also generated. This process is enhanced during phases II and III where exponential tails develop on

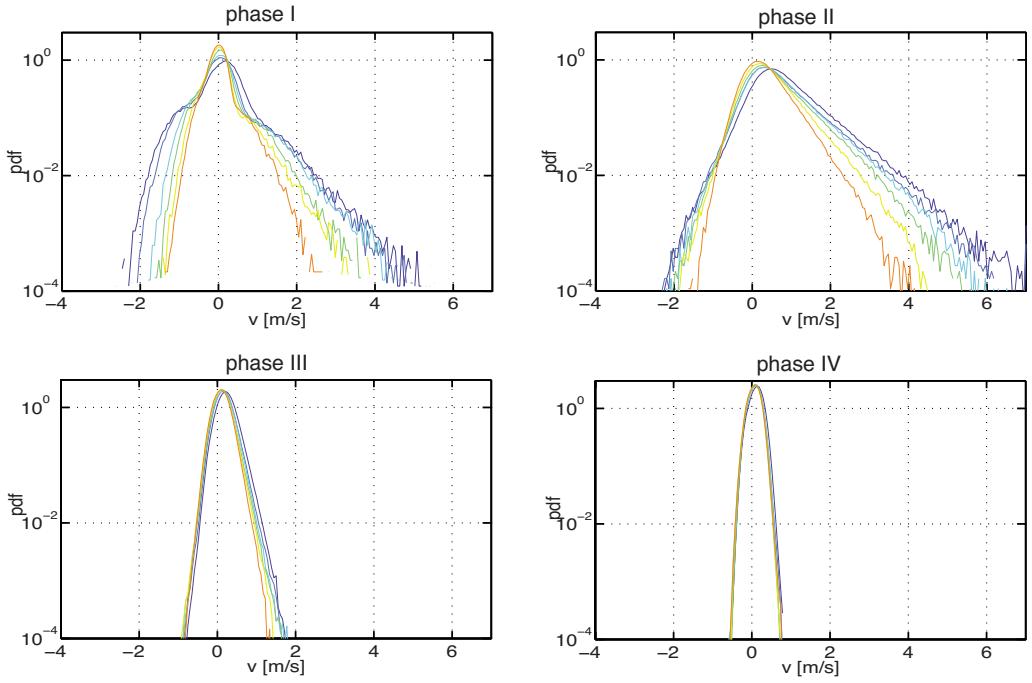

FIG. 11. (Color online) Velocity pdfs of the poloidal velocity during each phase of the flow evolution—defined in the text.

each side of the peak of the velocity distribution. One important observation is that during the development of the strongly anisotropic turbulence, very large velocity events are observed. When normalized to the rms value, distributions of phases I and II collapse onto single curves. For these anisotropic phases, the rms value scales linearly with the initial rotation rate. The exponential tails get narrower during the isotropization phase III while the center of distribution evolves toward Gaussianity. Full Gaussian pdfs are only recovered in the latest stages of decay, once isotropy has been restored.

IV. CONCLUSION

Measurements obtained with a two-axis potential probe show that after the fluid is set into motion by a combination of inertial and Coriolis forces, two phases of turbulence develop: A first one, strongly anisotropic, during which one observes the occurrence of very high velocity events (corresponding to exponential tails in the PDFs). We interpret these events as the advection over the probe of intense vorticity/helical structures generated in the near-wall region or in the bulk of the flow or both. This phase is followed by a quite sharp decrease in fluctuations after which the flow decays toward isotropic turbulence. We note in this process the faster isotropization of small scales.

These observations have interesting implications in the context of dynamo research, for which this flow has been considered by Frick *et al.*[4] As we have observed, the flow has a strongly anisotropic phase. In previous MHD studies this features has been enhanced by the presence of helical diverters inserted in a cross section of the torus.[4,14] Inspection of magnetic induction processes in the resulting flow have shown the possibility of α and β effects during limited time intervals.[14,15] Here α and β refer to mean-field MHD qantities,[16] and they account for the induction of electrical currents by small-scale helical motions (α) and for the added dissipation under the action of fluctuating velocity gradients (β). MHD measurements[14,15] have shown that these effects indeed occur, simultaneously and during the period recognized here as the existence of a strongly anisotropic turbulence. For instance, a small increase in magnetic diffusivity (β effect) occurs only during the anisotropic phase and decays sharply as the flow relaxes toward isotropy.

ACKNOWLEDGMENTS

We are grateful to M. Moulin and M. Tanase in their assistance for the development of the probe. G.V., N.P., and J.-F.P. thank the ICMM for their welcome during their stay in Perm. This work has been supported by CNRS-RFBR Grant No. 07-01-92160.

[1] J. M. Ottino, "Mixing, chaotic advection, and turbulence," Annu. Rev. Fluid Mech. **22**, 207 (1990).
[2] M. R. E. Proctor, "Effects of fluctuation on α-Ω dynamo models," Mon. Not. R. Astron. Soc. **382**, L39 (2007).1745-3933
[3] H. K. Moffatt, *Magnetic Field Generation in Electrically Conducting Fluids* (Cambridge University Press, Cambridge, 1978).
[4] P. Frick, V. Noskov, S. Denisov, S. Khripchenko, D. Sokoloff, R. Stepanov, and A. Sukhanovsky, "Non-stationary screw flow in a toroidal channel: Way to a laboratory dynamo experiment," Magnetohydrodynamics **38**, 136 (2002).
[5] S. Denisov, V. Noskov, A. Sukhanovskiy, and P. Frick, "Unsteady turbulent spiral flows in a circular channel," Fluid Dyn. **36**, 734 (2001).
[6] W. Dobler, P. Frick, and R. Stepanov, "The screw dynamo in a time-dependent pipe flow," Phys. Rev. E **67**, 056309 (2003).
[7] J.-L. Guermond, R. Laguerre, J. Léorat, and C. Nore, "An interior penalty Galerkin method for the MHD equations in heterogeneous domains," J. Comput. Phys. **221**, 349 (2007).
[8] R. Ricou and C. Vives, "Local velocity and temperature measurements in molten metals using an incorporated probe," Int. J. Heat Mass Transfer **25**, 1579 (1982).
[9] A. Tsinober, E. Kit, and M. Teitel, "On the relevance of the potential-difference method for turbulence measurements," J. Fluid Mech. **175**, 447 (1987).
[10] T. von Weissenfluh, "Probes for local velocity and temperature measurements in liquid metal flow," Int. J. Heat Mass Transfer **28**, 1563 (1985).
[11] A. Cramer, K. Varshney, T. Gundrum, and G. Gerberth, "Experimental study on the sensitivity and accuracy of electric potential local flow measurements," Flow Meas. Instrum. **17**, 1 (2006).
[12] M. Berhanu, B. Gallet, N. Mordant, and S. Fauve, "Reduction of velocity fluctuations in a turbulent flow of gallium by an external magnetic field," Phys. Rev. E **78**, 015302 (2008).
[13] W. R. Dean, Philos. Mag. **4**, 208 (1927); for a recent study, see A.Chupin and R. Stepanov, Phys. Rev. E **77**, 057301 (2008).
[14] R. Stepanov, R. Volk, V. Noskov, S. Denisov, P. Frick, and J.-F. Pinton, "Induction, helicity and alpha effect in a toroidal screw flow of liquid gallium," Phys. Rev. E **73**, 046310 (2006).
[15] S. Denisov, V. Noskov, R. Stepanov, and P. Frick, "Measurements of turbulent magnetic diffusivity in a liquid-gallium flow," JETP Lett. **88**, 167 (2008).
[16] K.-H. Rädler and R. Stepanov, "Mean electromotive force due to turbulence of a conducting fluid in the presence of mean flow," Phys. Rev. E **73**, 056311 (2006), and references therein.